Ore Geology Reviews 106 (2019) 226–237

Contents lists available at ScienceDirect

Ore Geology Reviews

journal homepage: www.elsevier.com/locate/oregeorev

# Timing of skarn gold deposition in the giant Beiya polymetallic gold deposit, southwest China: Constraints from in situ monazite SIMS U-Th-Pb geochronology

Haoyang Zhou[a,c,d], Xiaoming Sun[a,b,c,e,*], Zhongwei Wu[b,c], Qian Huang[a]

[a] School of Earth Sciences and Engineering, Sun Yat-sen University, Guangzhou 510275, China
[b] School of Marine Sciences, Sun Yat-sen University, Guangzhou 510006, China
[c] Guangdong Provincial Key Laboratory of Marine Resources and Coastal Engineering, Guangzhou 510275, China
[d] GFZ German Research Centre for Geosciences, Telegrafenberg, Potsdam 14473, Germany
[e] Southern Laboratory of Ocean Science and Engineering (Guangdong, Zhuhai), Zhuhai 519000, China

ARTICLE INFO

*Keywords:*
Hydrothermal monazite
SIMS U-Th-Pb dating
Beiya deposit
Skarn gold deposition

ABSTRACT

Robust dating of hydrothermal deposits is critical to understand ore genesis, which depends on judicious selection of mineralization-related chronometers, especially for complex polymetallic mineral systems. The Beiya deposit in southwest China is a world-class polymetallic gold system (11.9 Moz Au at a grade of 2.52 g/t) and the main mineralization is considered as skarn-type. However, available dating results for the gold mineralization give a wide range of ages, which in some cases could be inaccurate due to the use of non matrix-matched external isotope standards or an equivocal relationship between gold and the dated minerals. In this contribution, hydrothermal monazite coexisting with gold-bearing ore minerals (magnetite, pyrite and chalcopyrite) from high-grade massive magnetite-(sulfide) gold ores at Beiya was dated in situ using secondary ion mass spectrometry (SIMS). The U-Th-Pb analyses of hydrothermal monazite yielded a $^{208}Pb/^{232}Th$ age of 36.0 ± 0.5 Ma (2σ, MSWD = 2.0, n = 27), which is considered a robust age for the Beiya skarn gold mineralization. Our study supports a genetic link between the skarn gold mineralization and the post-collisional quartz monzonite magmatism at Beiya based on a new zircon U-Pb age of 37.2 ± 0.4 Ma. Compared with the previously-reported molybdenite Re-Os and sphalerite Rb-Sr isochron ages, our monazite U-Th-Pb result suggests that the gold deposition was broadly coeval with the formation of molybdenite but probably prior to the local Pb-Zn-Ag mineralization at Beiya.

## 1. Introduction

The timing of hydrothermal mineralization is critical to understanding the genesis of ore deposits (e.g., Morelli et al., 2007; Kempe et al., 2008; Westhues et al., 2016; Zhou et al., 2017b). However, suitable minerals for radiogenic isotope geochronometers are typically lacking in the common Fe-oxide/-sulfide ores, making it difficult to accurately date hydrothermal ore deposits (Arehart et al., 2003). In addition, mineralization events responsible for the formation of giant polymetallic mineral systems are complex and may involve multi-stage processes, which necessitates judicious selection of mineralization-related geochronometers and may require in-situ methods (e.g., Tretbar et al., 2000; Kirk et al., 2002; Selby et al., 2002; Pelleter et al., 2007; Rasmussen et al., 2007b, 2016; Meffre et al., 2016).

The world-class Beiya deposit, located in the Jinshajiang-Red River alkaline magmatic belt, southwest China, is one of the largest gold deposits in China (11.9 Moz Au @ 2.52 g/t; Mao et al., 2017) and it also contains substantial Fe-Cu-Pb-Zn-Ag resources. The deposit is spatially related to Cenozoic quartz monzonite porphyries and the main mineralization is considered as skarn-type based on mineralogy and alteration style (Deng et al., 2015a; He et al., 2015, 2016a; Li et al., 2016; Zhou et al., 2016, 2017a). Gold ores formed at Beiya are characterized by abundant magnetite and sulfides and the main host minerals for gold include magnetite, pyrite and chalcopyrite (Zhou et al., 2016, 2017a). It has been suggested that the quartz monzonite porphyry is responsible for the Beiya gold mineralization based on the correspondence of hydrothermal molybdenite Re-Os (38.1–34.7 Ma) and magmatic zircon U-Pb ages (37.9–34.7 Ma; He et al., 2013, 2015; Liu, 2014; Fu et al., 2015; Niu et al., 2015). This conclusion, however, needs to be tested because of the broad range of reported ages and the weak or ambiguous

* Corresponding author at: School of Earth Sciences and Engineering, Sun Yat-sen University, Guangzhou 510275, China.
*E-mail addresses:* hzhou@gfz-potsdam.de (H. Zhou), eessxm@mail.sysu.edu.cn (X. Sun).

https://doi.org/10.1016/j.oregeorev.2019.01.028
Received 26 September 2018; Received in revised form 14 December 2018; Accepted 31 January 2019
Available online 05 February 2019
0169-1368/ 

association between Au and Mo. Hence, it is urgent to provide a more robust age constraint on the Beiya skarn gold mineralization, to better understand relationships among gold deposition, molybdenite formation, and local magmatism.

Monazite is a common accessory mineral in a wide range of hydrothermal deposits and is highly resistant to weathering. This LREE-rich phosphate contains high U and Th contents and has a high blocking temperature (exceeding 700 °C; Parrish, 1990), making it a reliable dating mineral. Remarkably, monazite is commonly found in direct paragenetic association with gold precipitation in hydrothermal deposits (e.g., Rasmussen et al., 2007a; Sarma et al., 2011; Fielding et al., 2017). Furthermore, developments in analytical instruments [e.g., laser ablation inductively coupled plasma mass spectrometry (LA-ICP-MS), ion microprobe; Schoene, 2014], and an improved understanding of matrix effects (Fletcher et al., 2010; Li et al., 2013) allow high-precision, in-situ U-Th-Pb dating of monazite. In recent years, hydrothermal monazite has successfully constrained the ages of many important gold deposits worldwide, such as the Tom's Gully mine Australia (Rasmussen et al., 2006), the gold reefs in the Witwatersrand basin, South Africa (Rasmussen et al., 2007a), and the Hutti deposit in India (Sarma et al., 2008).

In this study, hydrothermal monazite was identified in the high-grade gold ores at Beiya and in-situ U-Th-Pb dating was carried out using secondary ion mass spectrometry (SIMS). Combining these results with our new zircon U-Pb age for the Beiya quartz monzonite porphyry and with previously reported chronological data from the deposit, we discuss the robust age determination for the Beiya skarn gold deposition and its temporal links to the quartz monzonite magmatism and polymetallic mineralization.

## 2. Geological background

### 2.1. Regional geology

The NW-trending Jinshajiang-Red River belt is a crustal-scale strike-slip fault zone separating the South China Block (comprising the Yangtze Craton and the Cathaysian Block) from the Indochina-Simao Block (Fig. 1). During the Middle to Late Triassic, diachronous closure of the eastern Paleo-Tethys created the Paleo-Tethyan Jinshajiang suture zone (Wang et al., 2000). Due to the extrusion tectonics caused by the post-India-Asia collision, reactivation of the Jinshajiang suture zone in the late-Oligocene–Miocene eventually formed the Jinshajiang-Red River belt (Schärer et al., 1990; Tapponnier et al., 1990; Chung et al., 1997; Yin and Harrison, 2000). Between 40 and 30 Ma, it was suggested that delamination below the overthickened crust resulted in the extensive potassic/alkaline felsic and mafic magmatism along the belt (e.g., porphyritic granitoids and lamprophyre dikes; Turner et al., 1996; Chung et al., 1997, 1998; Lu et al., 2012).

The Jinshajiang-Red River belt contains profuse alkaline porphyry-related Au-Cu-Mo deposits and has become one of the most important polymetallic metallogenic provinces in China (Hou et al., 2006; Deng et al., 2014). The alkaline porphyry-related Au-Cu-Mo mineralization is represented by two world-class ore systems, the Yulong porphyry Cu-(Mo) belt in the northern segment of the belt (9 Mt Cu; Liang et al., 2009) and the Beiya polymetallic Au deposit in the south (11.9 Moz Au; Mao et al., 2017).

The Beiya area is located to the east of the Jinshajiang-Red River fault at the western margin of Yangtze Craton, in the N-W trending Heqing-Songgui-Beiya syncline which encompasses the N-S trending Maanshan fault and an E-W trending concealed fault. The exposed stratigraphy in the Beiya area mainly consists of limestone from the Middle Triassic Beiya Formation, sandstone from the Lower Triassic Qingtianbao Formation, and continental flood basalt from the Upper Permian Emeishan Formation (Fig. 2). Porphyritic quartz monzonite and biotite monzonite are the main exposed alkaline granitoids. Other minor intrusions include lamprophyre dikes.

### 2.2. Deposit geology

The Beiya deposit covers an area ~6 km long and ~2–3 km wide, divided into six ore segments, i.e., Wandongshan, Hongnitang, Jingouba, Weiganpo, Bijiashan, and Guogaishan (Fig. 2). Besides the large gold resources, the deposit contains 200 Mt Fe @ 33.92%, 0.8 Mt Cu @ 0.61%, 1.55 Mt Pb @ 2.01%, 0.53 Mt Zn @ 1.38% and 8250 t Ag @ 51.90 g/t (Mao et al., 2017). Approximately 85% of total resources are hosted in the Wandongshan segment, where Fe-Au-Cu orebodies spatially related to the quartz monzonite porphyry are being exploited by open pit mining (Fig. 3A). The Hongnitang segment hosts minor Au-Fe-Cu resources, whereas the Bijiashan segment mainly includes Pb-Zn-Ag orebodies. Until now, no commercial orebodies have been found in the other three segments Weiganpo, Guogaishan, and Jingouba.

There are three mineralization styles developing at Beiya, including porphyry-, skarn-, and supergene-type. Porphyry mineralization is distributed at a limited scale in the Wandongshan and Hongnitang segments, producing Cu-Au-(Mo) resources in the form of auriferous quartz-sulfide veinlets crosscutting the quartz monzonite porphyries. The skarn-type is the main mineralization at Beiya, which is developed between the quartz monzonite porphyry and the Beiya Formation limestone. At Wandongshan, skarn mineralization has formed several massive Au-Fe-Cu orebodies, which include KT52, the largest gold orebody at Beiya with over 6.6 Moz Au (Li et al., 2016; Fig. 3). The shallow parts of the Au-Fe-Cu skarn-type orebodies have undergone extensive weathering and were mostly altered to limonite and jarosite. Polymetallic Cu-Fe-Pb-Zn-Ag orebodies, which can be considered as products of distal skarn mineralization, are present both along brittle fracture zones within the Beiya Formation and along the lithologic contact between the Beiya Formation and the Qingtianbao Formation (He et al., 2015, 2016a). Supergene-type mineralization is distributed at the unconformity between the Triassic Beiya Formation limestone and the Quaternary glutenite, conglomerate, and clays. An example of this type is KT4 (Fig. 3B), an Fe-Au orebody in which massive magnetite relicts could be found.

The Beiya skarn mineralization can be divided into prograde and retrograde stages. During the prograde stage, andradite-rich garnet and diopside crystalized, whereas in the retrograde stage, hydrous minerals (e.g., chlorite, amphibole, epidote, sericite and biotite-phlogopite) were formed, accompanied by the successive crystallization of oxide minerals (dominated by magnetite and minor hematite) and then sulfide phases (dominated by pyrite and chalcopyrite, and minor galena and sphalerite). Intensive retrograde alteration formed the commercial ores at Beiya, i.e., massive magnetite Fe-Au and magnetite-sulfide Fe-Au-Cu ores (Fig. 4A, B). It has been suggested that gold precipitation is contemporaneous with the formation of oxide- and sulfide-minerals in the retrograde-stage (Zhou et al., 2016, 2017a). Magnetite contains abundant nano- to micron-sized gold particles (Fig. 4C and more detail in Zhou et al., 2017a). With respect to sulfide minerals, gold is mainly hosted by pyrite and chalcopyrite (Fig. 4D, E). Molybdenite is locally found within a silicate skarn assemblage (e.g., garnet, diopside, chlorite and epidote) and not in the typical gold ores.

## 3. Samples and analytical methods

### 3.1. LA-ICP-MS U-Pb dating of zircon

For dating the magmatism, two samples of the quartz monzonite porphyry were collected from the Wandongshan open pit to extract zircon grains. Zircon grains were separated by crushing, magnetic and hydro-separation, followed by hand-picking under a binocular microscope. Selected zircon grains were mounted in epoxy resin. Before U-Pb isotope analysis, the internal textures of zircon were investigated via cathodoluminescence (CL) imaging at the School of Earth Sciences and Engineering, Sun Yat-sen University (SYSU).

Zircon U-Pb dating was performed using LA-ICP-MS at the

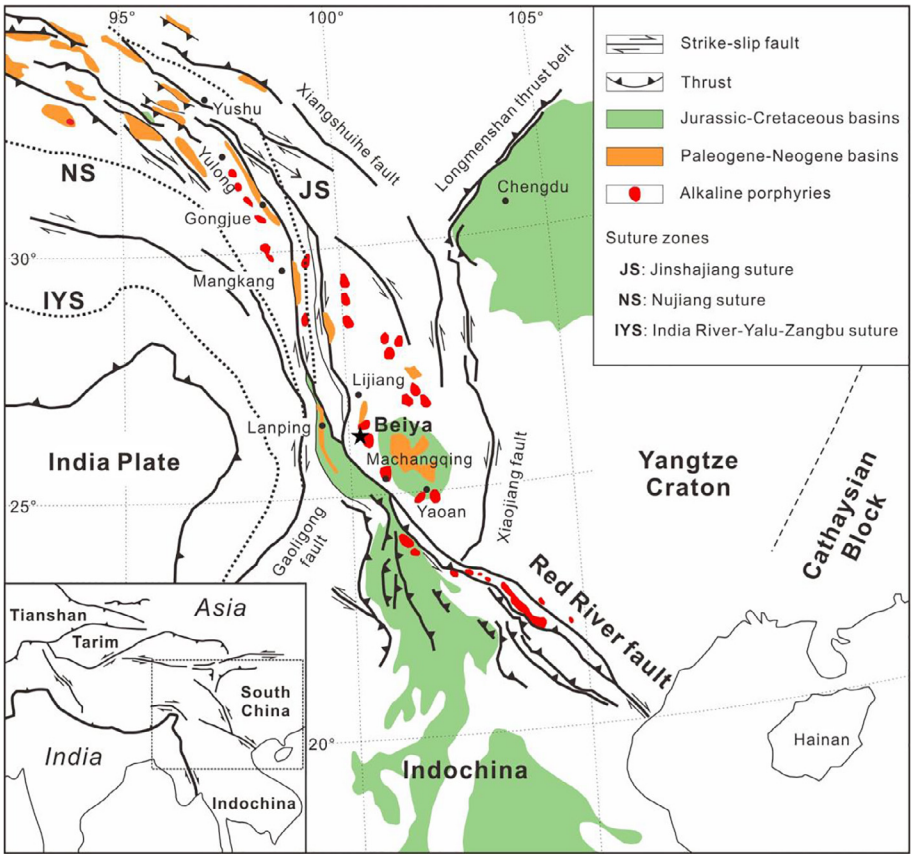


**Fig. 1.** Tectonic outline of the Jinshajiang-Red River alkaline magmatic belt in southwest China (modified after Wang et al. (2001) and Hou et al. (2004)).

Guangdong Provincial Key Laboratory of Marine Resources and Coastal Engineering, SYSU. The instrumental setup and analytical conditions are given in Table 1. Zircon 91,500 was used as an external standard to determine U-Pb isotope fractionation and mass discrimination. Time-drift correction was based on a linear interpolation method according to the multiple analyses of zircon 91,500. Lead, Th, and U concentrations of zircon were determined using NIST SRM610 as an external standard and Si content as internal standard. Data were processed using the ICPMSDataCal software (Liu et al., 2010). The reference zircon Plešovice was applied as a secondary standard. The weighted mean $^{206}Pb/^{238}U$ age of 338.2 ± 3.4 Ma (2σ, MSWD = 0.088, n = 7) for Plešovice in this study agrees well with its ID-TIMS age (337.13 ± 0.37 Ma; Sláma et al., 2008). Concordia diagrams and weighted mean ages were produced using the ISOPLOT add-in (Ludwig,

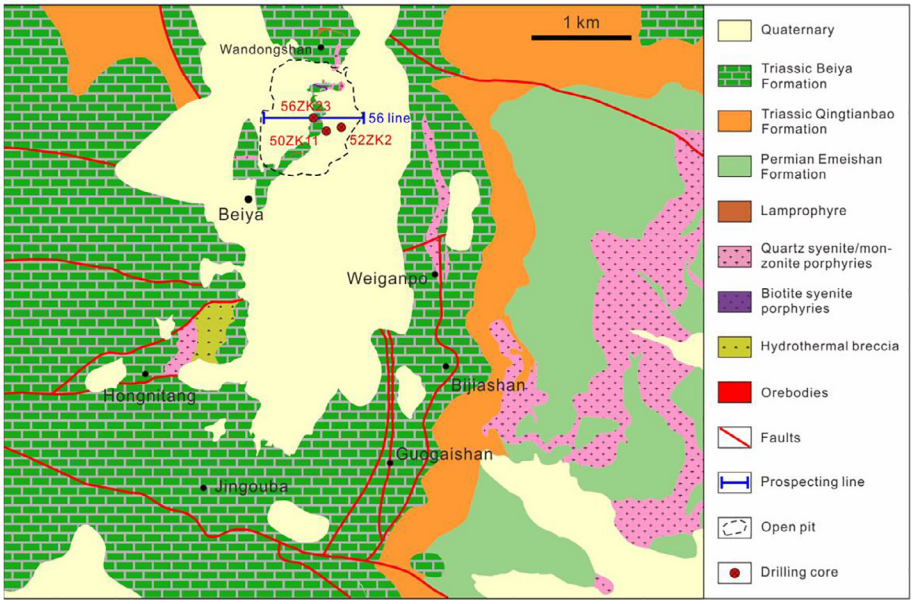


**Fig. 2.** Geological map showing the distribution of strata, intrusions, major faults, drilling cores, and the contour of the Wandongshan open pit in the Beiya area (modified after Yunnan Gold & Mineral Group Co., Ltd (2013)).

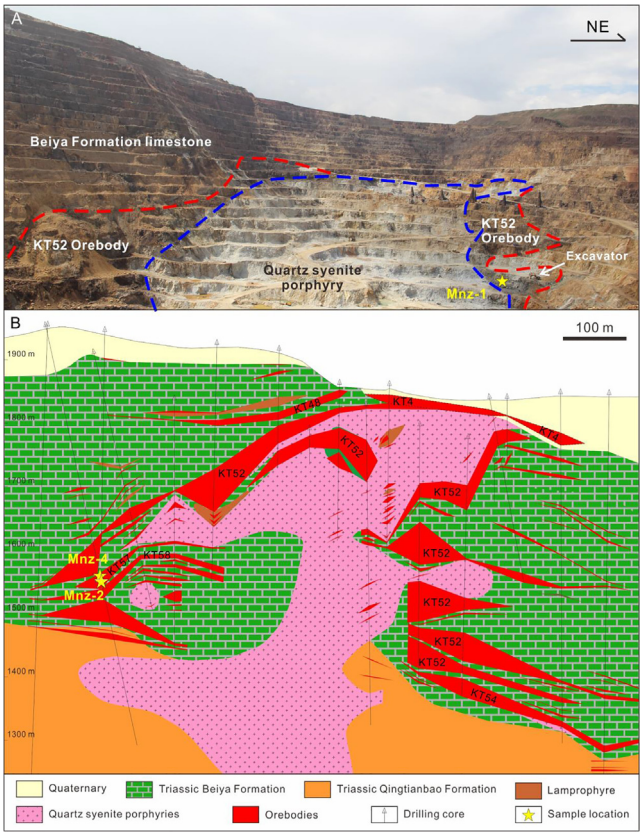


**Fig. 3.** (A) Photograph showing the northwest part of the Wandongshan open pit. (B) Cross section of prospecting line 56 showing the distribution of orebodies in the Wandongshan segment (modified after Yunnan Gold & Mineral Group Co., Ltd (2013)).

2003).

### 3.2. SIMS U-Th-Pb dating of monazite

Five representative ore samples (Fig. 4A, B), comprising high-grade massive magnetite and magnetite-sulfide gold ores, were collected from the Wandongshan open pit and drilling cores to prepare polished thin sections. Sample locations and detailed descriptions are shown in Figs. 2 and 3 and Table 2. Mineralogy and textures of the ore samples were investigated under optical microscope and further examined via backscattered electron (BSE) imaging using a TESCAN VEGA II LMU scanning electron microscope (SEM) equipped with INCA Penta FET × 3 energy-dispersive spectrometer (EDS) at the Key Laboratory of Marine Mineral Resources, Guangzhou Marine Geological Survey, and a ZEISS ΣIGMA SEM equipped with INCA X-MAX020 EDS at the School of Earth Sciences and Engineering, SYSU. Cylinders containing monazite were extracted from the thin sections using microdrilling and were then mounted along with monazite standards in epoxy resin for SIMS analysis.

In situ monazite SIMS U-Th-Pb dating was conducted using a Cameca IMS-1280 SIMS at the Institute of Geology and Geophysics, Chinese Academy of Sciences in Beijing. The instrument description and operating protocol applied to monazite have been detailed in Li et al. (2013). A primary beam of $O_2^-$ ion produced an elliptic spot (~15 × 10 μm) on the monazite surface. Positive secondary ions were extracted under a 10-kV potential. To separate $Pb^+$ peaks from isobaric interferences, a 60-eV energy window together with a mass resolution of ~5400 (at 10% peak height) was used in the secondary ion beam optics. A single electron multiplier was used in ion-counting mode to measure secondary ion beam intensities by peak jumping mode. Each measurement consisted of 7 cycles. Monazite RW-1 ($^{207}Pb/^{235}U$ age = 904.15 ± 0.26 Ma [2σ], Th = 11.8 ± 1.0 wt% [2σ], and Th/U = 42.5 ± 3.0 [2σ]; Ling et al., 2017) was interspersed with unknowns as the standard to calibrate U and Th concentrations and U-Th-Pb isotope ratios. A repeatability of 1.5% (1σ RSD) was derived from long-term $^{206}Pb/^{238}U$ measurement of the monazite standard. As a

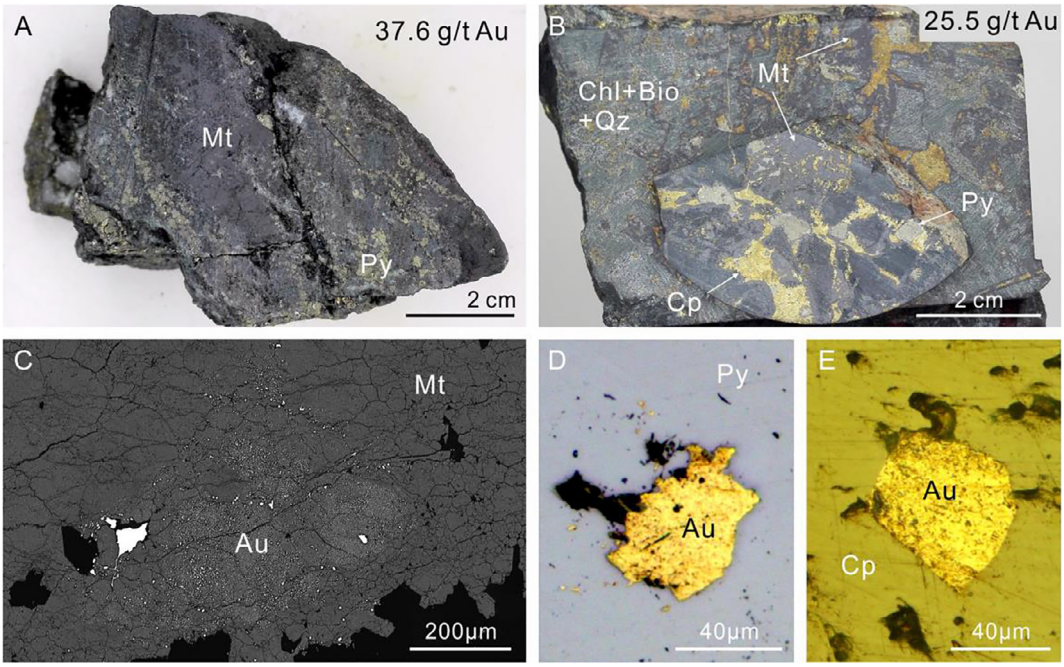


**Fig. 4.** Photomicrographs showing typical high-grade gold ores and their gold occurrence in the Wandongshan segment, Beiya. (A) Massive magnetite (Mt) Fe-Au ore with minor pyrite (Py; sample Mnz-1). (B) Massive magnetite-sulfide Fe-Au-Cu ore with chlorite (Chl), biotite (Bio), and quartz (Qz; sample Mnz-4). (C) BSE image illustrating abundant nano- to micro-sized gold (Au) particles hosted by magnetite. (D, E) Reflected light images illustrating gold inclusions in pyrite and chalcopyrite (Cp).

**Table 1**
Instrumental setup and operating conditions of LA-ICP-MS zircon U-Pb dating used in this study.

| | |
|---|---|
| *Laser ablation system* | |
| Laser system | GeoLasPro ArF-excimer laser ablation system |
| Laser wavelength | 193 nm |
| Pulse width | 15 ns |
| Energy density | 5 J/cm$^2$ |
| Fluence | 5 Hz |
| Ablation styles | Single spot |
| Spot size | 32 μm |
| Carrier gas | He 0.6–0.7 l/min |
| *ICP parameters* | |
| ICPMS | Agilent 7700× |
| RF power | 1550 W |
| Gas flows | Coolant: Ar 16 l/min, sample: Ar 0.8 l/min |
| *Acquisition parameters* | |
| Scanning model | Peak hopping, 1 point per peak |
| Acquisition model | Time resolved |
| Analysis time | ~20-s blank, 45-s ablation |
| Dwell times for zircon | 20 ms for $^{204}$Pb, $^{206}$Pb, $^{207}$Pb, $^{208}$Pb, 10 ms for $^{232}$Th, $^{238}$U |

measure of the accuracy of SIMS U-Th-Pb monazite analyses calibrated against RW-1 standard, monazite 44,069 was employed as a secondary standard. A concordia age of 422.4 ± 3.3 Ma is obtained for monazite 44,069, which agrees with the recommended value of 424.9 ± 0.4 Ma (Aleinikoff et al., 2006). For monazite SIMS analysis, the $^{204}$Pb-based common Pb correction is inappropriate because of large analytical uncertainty owing to low $^{204}$Pb concentrations and the probability of isobaric interferences derived from $^{232}Th^{144}Nd^{16}O_2^{2+}$ (Williams, 1998; Li et al., 2013). Therefore, a $^{207}$Pb-based correction (Williams, 1998; Li et al., 2013) was done to subtract common Pb (initial Pb) using the terrestrial Pb isotope composition for the corresponding ages (Stacey and Kramers, 1975). Age calculations and plots were performed with the ISOPLOT add-in (Ludwig, 2003).

## 4. Results

### 4.1. Zircon and U-Pb dates

Zircon grains from the Wandongshan quartz monzonite porphyry are mostly euhedral, ranging from ~50 to 200 μm in length and from ~50 to 100 μm in width. In the CL images, they are relatively dark gray to black (Fig. 5). Most grains show oscillatory zoning, although some of them contain inherited cores. The results of 22 analyses are listed in Table 3. The zircon contains 10–8693 ppm Th and 380–3933 ppm U. Most grains have Th/U ratios in the range of ~0.4–3.0. Their concordant $^{206}$Pb/$^{238}$U ages vary between 38.8 ± 1.4 and 35.9 ± 0.6 Ma (1σ), yielding a weighted mean age of 37.2 ± 0.4 Ma (2σ, MSWD = 1.2; Fig. 6).

### 4.2. Monazite and U-Th-Pb dates

The irregular-shaped monazite grains are ~10–50 μm in size and closely associated with both magnetite (Fig. 7A, B) and sulfide minerals (e.g., pyrite and chalcopyrite; Fig. 7C). Monazite also occurs as inclusions in pyrite and chalcopyrite (Fig. 7D, H). Also, tiny inclusions of magnetite and chalcopyrite appear in monazite grains (Fig. 7E). In some areas, monazite aggregates intergrown with magnetite occur in a chlorite + quartz matrix (Fig. 7F) or with chalcopyrite in a chlorite + biotite matrix (Fig. 7G). No visible inhomogeneity of monazite composition is apparent under the SEM-BSE. Locally, monazite occurs together with xenotime intergrowths in the ores (Fig. 7H).

The SIMS results of U-Th-Pb contents and isotope ratios of the Beiya monazite are shown in Table 4. The monazite grains contain variable U contents (35–333 ppm) and a larger range of Th concentrations (23–4822 ppm), giving Th/U ratios of 0.2–73.2. On the Tera-Wasserburg plot (Fig. 8), a line defined by 29 uncorrected $^{206}$Pb/$^{238}$U and $^{207}$Pb/$^{206}$Pb data gives a lower intercept $^{206}$Pb/$^{238}$U age of 35.6 ± 1.2 Ma and an initial $^{207}$Pb/$^{206}$Pb ratio of 0.849 ± 0.031 (MSWD = 3.1). After applying the $^{207}$Pb-based correction for common Pb, the weighted mean $^{206}$Pb/$^{238}$U age is 35.3 ± 0.9 Ma (2σ, MSWD = 1.8; Fig. 9A). Twenty-seven common Pb- corrected $^{208}$Pb/$^{232}$Th ages give a weighted mean of 36.0 ± 0.5 Ma (2σ, MSWD = 2.0; Fig. 9B), with two spots (Mnz-1-03 and Mnz-3-02) being rejected as outliers.

## 5. Discussion

### 5.1. Origin of monazite

Monazite commonly occurs as an accessory mineral in various hydrothermal deposits. Hydrothermal monazite characteristically coexists with other hydrothermal minerals, forms local accumulations in a small area, and contains low $ThO_2$ content (typically < 1 wt%), in distinction to igneous monazite that has high $ThO_2$ contents of 3– > 5 wt% (Schandl and Gorton, 2004). The Beiya monazite is commonly intergrown with major ore minerals (e.g., magnetite, pyrite and chalcopyrite) and hydrous retrograde skarn minerals (e.g., chlorite and biotite). The monazite is characterized by patchy distribution with high local abundance, it has low Th contents (< 0.5 wt%) and is thus interpreted as hydrothermal in origin.

Hydrothermal monazite was also identified in the Yaoan gold deposit, which is located to the southeast of Beiya in the Jinshajiang-Red River belt (Fig. 1) and characterized by abundant hematite-rich auriferous veins related to a syenite porphyry (Zhou et al., 2017b). For comparison, we plotted the U and Th concentrations of the monazite from Beiya together with published compositions of the hydrothermal monazite from Yaoan (Fig. 10). It is seen that the monazite from the two locations have similar Th contents, whereas the U concentrations and Th/U ratios of the Beiya monazite are lower than those of the Yaoan counterpart. This could be caused by different Th-U contents in

**Table 2**
Location and description of samples for monazite dating.

| Sample | Location | Description |
|---|---|---|
| Mnz-1 | KT52 orebody in the Wandongshan open pit, NE of the quartz monzonite porphyry, 26°10′12.6″ N, 100°11′29.3″ E | Massive magnetite gold ore with minor pyrite; Au grade: 37.6 g/t |
| Mnz-2 | Wandongshan drilling core, 56ZK23, 412-m depth | Massive magnetite-pyrite-chalcopyrite gold ore with chlorite; Au grade: 6 g/t |
| Mnz-3 | Wandongshan drilling core, 50ZK11, 192-m depth | Massive magnetite-pyrite gold ore with chlorite; no grade data but native gold observed |
| Mnz-4 | Wandongshan drilling core, 56ZK23, 402-m depth | Magnetite-pyrite-chalcopyrite ore with chlorite and biotite; Au grade: 25.5 g/t |
| Mnz-5 | KT52 orebody in the Wandongshan drilling core, 52ZK2, unknown depth | Massive magnetite gold ore with minor pyrite; no grade data but native gold observed |

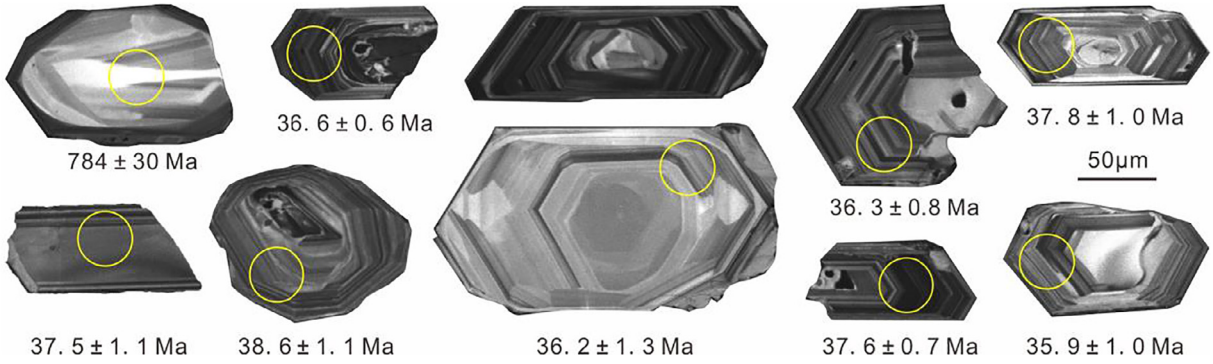


**Fig. 5.** CL images showing internal textures and $^{206}Pb/^{238}U$ ages (1σ) of zircon grains from the quartz monzonite porphyry at Wandongshan, Beiya.

the hydrothermal fluids, or, more likely, by different redox conditions of the hydrothermal fluids. Oxidizing condition would favor the formation of monazite with high Th/U ratios (Janots et al., 2012) because Th is always present as tetravalent valence and can be incorporated into monazite by substituting for rare earth elements (REEs), whereas U can occur as $U^{4+}$ or $U^{6+}$ depending on the redox condition and only tetravalent U (at lower oxygen fugacity) can substitute for REEs (van Emden et al., 1997; Janots et al., 2012). A difference in redox conditions is consistent with the dominance of magnetite in the Beiya ores and the dominance of hematite in the Yaoan ores, and with diverse Bi-Te-mineral assemblages in the two deposits (Zhou et al., 2016, 2018).

### 5.2. Interpretation of monazite ages

Lead is relatively incompatible in the crystal structure of monazite. For young samples with low radiogenic Pb accumulations, however, the contribution of initial Pb in monazite can be significant, making an impact on age calculation (e.g., Janots et al., 2012; Harlan et al., 2017). The fraction of initial Pb could be illustrated in a Tera-Wasserburg plot, where positions of those analyses with high levels of initial Pb are closer to the Y-axis intercept of the regression. The fraction of initial $^{206}Pb$ ($f_{206}$) can be further evaluated using the following equation (Williams, 1998):

$$f_{206} = \frac{^{207}Pb/^{206}Pb_T - ^{207}pb/^{206}Pb}{^{207}Pb/^{206}Pb_c - ^{207}Pb/^{206}Pb} \times 100\%$$

where $^{207}Pb/^{206}Pb_T$ is the total (measured) $^{207}Pb/^{206}Pb$ ratio, $^{207}Pb/^{206}Pb^*$ is the assumed uranogenic $^{207}Pb/^{206}Pb$ ratio, and $^{207}Pb/^{206}Pb_c$ is the common $^{207}Pb/^{206}Pb$ ratio derived from the terrestrial Pb evolution model (Stacey and Kramers, 1975).

Our calculation indicates that the Beiya monazite contains $f_{206}$ in the range of 5–89%. The corrected $^{206}Pb/^{238}U$ ages thus have large uncertainties but give a weighted mean of 35.3 ± 0.9 Ma. This age, within uncertainty, is identical to the lower intercept of 35.6 ± 1.2 Ma in the Tera-Wasserburg plot, which confirms the reliability of the $^{207}Pb$ correction method.

However, for young monazites, the $^{208}Pb/^{232}Th$ age is recommended as more robust (Bosse et al., 2009; Janots et al., 2012; Schulze et al., 2015). This is because when compared to $^{206}Pb/^{238}U$, the $^{208}Pb/^{232}Th$ age is less sensitive to the involvement of common Pb due to the abundance of radiogenic $^{208}Pb$ (originating from $^{232}Th$) over $^{206}Pb$ (originating from $^{238}U$) in monazite that contains high Th relative to U. The fraction of initial $^{208}Pb$ ($f_{208}$) can be calculated as (Janots et al., 2012):

$$f_{208} = \frac{^{208}Pb/^{206}Pb_c}{^{208}Pb/^{206}Pb_T} \times f_{206}$$

where $^{208}Pb/^{206}Pb_c$ is based on the common $^{208}Pb/^{206}Pb$ ratio of the

**Table 3**
LA-ICP-MS U-Pb isotopes of zircon from the quartz monzonite porphyry at Wandongshan, Beiya.

| Spot | Pb | Th | U | Th/U | Measured isotope ratios | | | | | | Calculated ages (Ma) | | | | Concordance |
|---|---|---|---|---|---|---|---|---|---|---|---|---|---|---|---|
| | ppm | ppm | ppm | | $^{207}Pb/^{206}Pb$ | σ | $^{207}Pb/^{235}U$ | σ | $^{206}Pb/^{238}U$ | σ | $^{207}Pb/^{235}U$ | σ | $^{206}Pb/^{238}U$ | σ | |
| Zrc-01 | 22.7 | 4017 | 1335 | 3.01 | 0.0544 | 0.0040 | 0.0003 | 0.0030 | 0.0058 | 0.0001 | 43.0 | 2.9 | 37.5 | 0.6 | 86% |
| Zrc-02 | 29.5 | 5110 | 1983 | 2.58 | 0.0479 | 0.0040 | 0.0380 | 0.0030 | 0.0058 | 0.0001 | 37.8 | 2.9 | 37.6 | 0.7 | 99% |
| Zrc-03 | 6.5 | 903 | 561 | 1.61 | 0.0518 | 0.0069 | 0.0390 | 0.0042 | 0.0059 | 0.0002 | 38.8 | 4.2 | 37.8 | 1.0 | 97% |
| Zrc-04 | 6.9 | 474 | 1066 | 0.44 | 0.0450 | 0.0039 | 0.0358 | 0.0031 | 0.0057 | 0.0001 | 35.7‘ | 3.1 | 36.3 | 0.8 | 98% |
| Zrc-05 | 4.9 | 493 | 602 | 0.82 | 0.0542 | 0.0064 | 0.0413 | 0.0045 | 0.0058 | 0.0002 | 41.1 | 4.3 | 37.5 | 1.1 | 90% |
| Zrc-06 | 36.3 | 5996 | 2537 | 2.36 | 0.0539 | 0.0031 | 0.0428 | 0.0025 | 0.0057 | 0.0001 | 42.5 | 2.4 | 36.4 | 0.6 | 84% |
| Zrc-07 | 47.6 | 8693 | 2911 | 2.99 | 0.0493 | 0.0031 | 0.0379 | 0.0021 | 0.0057 | 0.0001 | 37.8 | 2.1 | 36.3 | 0.6 | 96% |
| Zrc-08 | 23.0 | 3430 | 1802 | 1.90 | 0.0550 | 0.0038 | 0.0439 | 0.0027 | 0.0058 | 0.0001 | 43.6 | 2.6 | 37.4 | 0.6 | 84% |
| Zrc-09 | 20.1 | 1873 | 2499 | 0.75 | 0.0472 | 0.0030 | 0.0368 | 0.0022 | 0.0057 | 0.0001 | 36.7 | 2.2 | 36.6 | 0.6 | 99% |
| Zrc-10 | 7.3 | 578 | 926 | 0.62 | 0.0513 | 0.0042 | 0.0407 | 0.0030 | 0.0060 | 0.0002 | 40.5 | 3.0 | 38.6 | 1.1 | 95% |
| Zrc-11 | 3.6 | 238 | 553 | 0.43 | 0.0551 | 0.0070 | 0.0393 | 0.0046 | 0.0058 | 0.0002 | 39.2 | 4.5 | 37.5 | 1.4 | 95% |
| Zrc-12 | 2.3 | 178 | 380 | 0.47 | 0.0703 | 0.0115 | 0.0439 | 0.0063 | 0.0056 | 0.0002 | 43.6 | 6.1 | 36.2 | 1.3 | 81% |
| Zrc-13 | 8.2 | 817 | 1063 | 0.77 | 0.0503 | 0.0045 | 0.0384 | 0.0032 | 0.0057 | 0.0001 | 38.3 | 3.1 | 36.5 | 0.9 | 95% |
| Zrc-14 | 8.3 | 895 | 694 | 1.29 | 0.0559 | 0.0051 | 0.0468 | 0.0040 | 0.0060 | 0.0001 | 46.4 | 3.9 | 38.5 | 0.9 | 81% |
| Zrc-15 | 10.8 | 1419 | 948 | 1.50 | 0.0497 | 0.0048 | 0.0368 | 0.0032 | 0.0056 | 0.0002 | 36.7 | 3.1 | 35.9 | 1.0 | 97% |
| Zrc-16 | 38.2 | 4167 | 3933 | 1.06 | 0.0492 | 0.0035 | 0.0394 | 0.0028 | 0.0057 | 0.0001 | 39.2 | 2.7 | 36.8 | 0.7 | 93% |
| Zrc-17 | 43.4 | 10 | 998 | 0.01 | 0.0492 | 0.0046 | 0.0387 | 0.0033 | 0.0060 | 0.0001 | 38.6 | 3.2 | 38.8 | 0.8 | 99% |
| Zrc-18 | 9.8 | 958 | 1107 | 0.87 | 0.0528 | 0.0046 | 0.0400 | 0.0032 | 0.0057 | 0.0001 | 39.8 | 3.1 | 36.7 | 0.7 | 91% |
| Zrc-19 | 10.4 | 817 | 1255 | 0.65 | 0.0566 | 0.0042 | 0.0413 | 0.0026 | 0.0057 | 0.0001 | 41.1 | 2.6 | 36.5 | 0.7 | 88% |
| Zrc-20 | 33.4 | 4667 | 2064 | 2.26 | 0.0529 | 0.0034 | 0.0421 | 0.0026 | 0.0059 | 0.0001 | 41.9 | 2.5 | 38.0 | 0.7 | 90% |
| Zrc-21 | 15.1 | 1866 | 1387 | 1.35 | 0.0479 | 0.0041 | 0.0367 | 0.0029 | 0.0058 | 0.0001 | 36.6 | 2.9 | 37.1 | 0.7 | 98% |
| Zrc-22 | 15.2 | 1752 | 1531 | 1.14 | 0.0453 | 0.0039 | 0.0374 | 0.0032 | 0.0060 | 0.0001 | 37.3 | 3.2 | 38.8 | 0.8 | 96% |

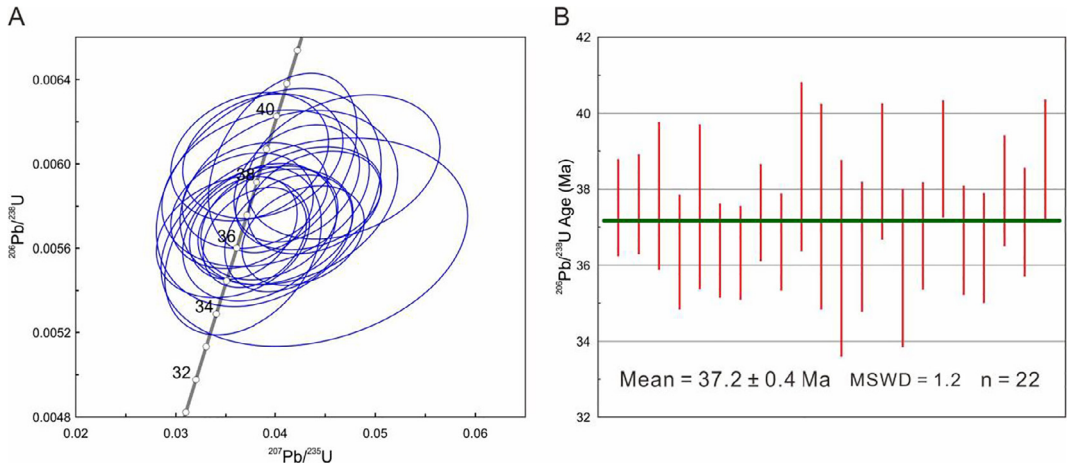


**Fig. 6.** Concordia diagram (A) and weighted mean $^{206}Pb/^{238}U$ age (B) of zircon from the quartz monzonite porphyry at Beiya (data-point uncertainties are 2σ).

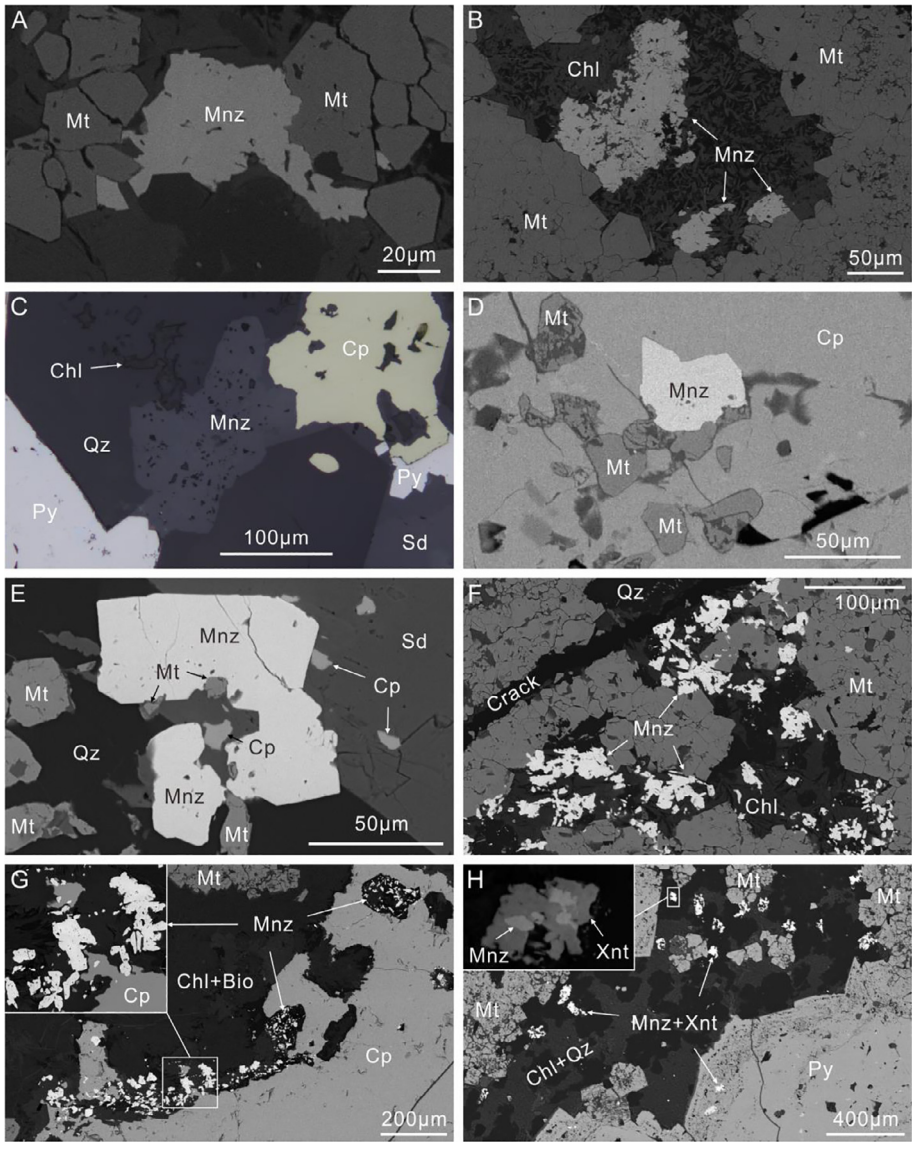


**Fig. 7.** Photomicrographs showing monazite (Mnz) occurrence and its relationship with gold-hosting ore minerals. (A) Coexistence of monazite with granular magnetite (Mt). (B) Irregular-shaped monazite coexisting with abundant magnetite in a chlorite (Chl) matrix. (C) Intergrowths of monazite with chalcopyrite, pyrite, quartz, and chlorite. (D) Coexistence of monazite and magnetite as inclusions in chalcopyrite. (E) Granular monazite with magnetite and chalcopyrite inclusions. (F) Monazite aggregates intergrown by chlorite and quartz (Qz) coexisting with magnetite. (G) Fine-grained monazite aggregates in a chlorite and biotite (Bio) matrix surrounded by chalcopyrite. (H) Phosphate intergrowths consisted of monazite and xenotime (Xnt) appearing as inclusions in pyrite or coexisting with magnetite. Figure C is under reflected light, while others are BSE images. Other abbreviations: Sd = siderite.

terrestrial Pb evolution model (Stacey and Kramers, 1975), and $^{208}Pb/^{206}Pb_T$ represents the total (measured) $^{208}Pb/^{206}Pb$ ratio. Our results indicate that about two-thirds of the Beiya monazite grains contain smaller $f_{208}$ than $f_{206}$. Overall, the corrected $^{208}Pb/^{238}Th$ ages have smaller uncertainties.

Furthermore, we consider the $^{208}Pb/^{232}Th$ ages more robust because of additional bias on $^{206}Pb/^{238}U$ ages resulting from excess $^{206}Pb$. This results from the fact that monazite strongly incorporates Th relative to

**Table 4**
In situ SIMS U-Th-Pb isotopes of the hydrothermal monazite from the Beiya gold deposit.

| Spot n = 29 | U | Th | Th/U | Measured isotope ratios | | | | | | $f_{206}$ | $f_{208}$ | $^{207}$Pb-correted ages (Ma) | | | |
|---|---|---|---|---|---|---|---|---|---|---|---|---|---|---|---|
| | ppm | ppm | | $^{208}$Pb/$^{206}$Pb | σ (%) | $^{206}$Pb/$^{238}$U | σ (%) | $^{207}$Pb/$^{206}$Pb | σ (%) | | | $^{206}$Pb/$^{238}$U | σ | $^{208}$Pb/$^{232}$Th | σ |
| Mnz-1-01 | 217 | 555 | 2.6 | 1.2662 | 4.26 | 0.0095 | 3.56 | 0.3536 | 5.31 | 39 | 63 | 37.1 | 2.5 | 33.0 | 1.5 |
| Mnz-1-02 | 325 | 4822 | 14.8 | 3.2389 | 2.40 | 0.0112 | 3.44 | 0.4606 | 3.21 | 52 | 33 | 34.1 | 3.0 | 35.7 | 0.6 |
| Mnz-1-03 | 317 | 3229 | 10.2 | 2.6582 | 3.72 | 0.0060 | 2.50 | 0.0903 | 5.22 | 6 | 4 | 36.7 | 1.0 | 29.0 | 0.8 |
| Mnz-1-04 | 175 | 4234 | 24.2 | 3.9535 | 2.46 | 0.0166 | 2.28 | 0.5642 | 2.81 | 65 | 34 | 36.8 | 5.0 | 37.7 | 0.6 |
| Mnz-1-05 | 186 | 1711 | 9.2 | 2.6746 | 4.94 | 0.0062 | 4.59 | 0.1631 | 3.63 | 15 | 11 | 33.8 | 1.6 | 34.6 | 0.9 |
| Mnz-1-06 | 94 | 4567 | 48.5 | 8.7451 | 4.63 | 0.0106 | 1.99 | 0.3942 | 5.13 | 44 | 10 | 38.1 | 2.7 | 35.3 | 0.6 |
| Mnz-1-07 | 230 | 4567 | 19.9 | 3.7171 | 2.13 | 0.0142 | 1.26 | 0.5470 | 2.55 | 63 | 35 | 33.4 | 4.0 | 35.7 | 0.6 |
| Mnz-1-08 | 149 | 4614 | 31.0 | 4.4814 | 2.63 | 0.0171 | 3.05 | 0.6276 | 1.15 | 73 | 34 | 28.9 | 5.3 | 37.3 | 1.7 |
| Mnz-1-09 | 98 | 4001 | 40.8 | 8.3373 | 3.91 | 0.0093 | 4.19 | 0.3168 | 6.04 | 34 | 8 | 39.1 | 2.5 | 37.0 | 0.7 |
| Mnz-1-10 | 134 | 3758 | 28.1 | 3.3823 | 2.83 | 0.0289 | 4.22 | 0.6780 | 1.97 | 80 | 49 | 37.0 | 10.0 | 36.5 | 1.0 |
| Mnz-1-11 | 178 | 2606 | 14.7 | 3.6716 | 3.35 | 0.0089 | 4.04 | 0.3762 | 6.99 | 42 | 23 | 33.5 | 2.8 | 37.1 | 0.9 |
| Mnz-1-12 | 100 | 3780 | 37.8 | 3.2325 | 1.85 | 0.0466 | 2.88 | 0.7515 | 2.70 | 89 | 57 | 31.7 | 18.7 | 34.9 | 0.8 |
| Mnz-2-01 | 88 | 596 | 6.7 | 2.1191 | 5.71 | 0.0065 | 3.52 | 0.1986 | 4.92 | 19 | 19 | 33.5 | 1.4 | 35.4 | 1.5 |
| Mnz-2-02 | 132 | 123 | 0.9 | 0.8053 | 5.86 | 0.0077 | 3.34 | 0.2711 | 3.70 | 28 | 73 | 35.4 | 1.6 | 36.1 | 1.9 |
| Mnz-2-03 | 151 | 506 | 3.4 | 1.1479 | 5.33 | 0.0064 | 3.23 | 0.1431 | 7.83 | 12 | 22 | 36.2 | 1.3 | 35.5 | 1.6 |
| Mnz-2-04 | 156 | 350 | 2.2 | 1.8789 | 2.37 | 0.0296 | 3.96 | 0.7043 | 2.29 | 83 | 91 | 31.5 | 10.8 | 36.3 | 2.7 |
| Mnz-2-05 | 185 | 1126 | 6.1 | 1.9791 | 5.93 | 0.0069 | 5.71 | 0.1399 | 9.39 | 12 | 12 | 39.0 | 2.4 | 36.2 | 1.2 |
| Mnz-2-06 | 332 | 1749 | 5.3 | 1.6164 | 3.47 | 0.0061 | 2.99 | 0.0852 | 6.23 | 5 | 6 | 37.3 | 1.2 | 36.2 | 1.4 |
| Mnz-2-07 | 301 | 935 | 3.1 | 1.0865 | 4.06 | 0.0059 | 1.79 | 0.1432 | 5.39 | 12 | 23 | 33.2 | 0.8 | 34.6 | 1.2 |
| Mnz-2-08 | 176 | 4182 | 23.7 | 5.6271 | 7.40 | 0.0089 | 8.57 | 0.3244 | 18.62 | 35 | 13 | 37.1 | 5.6 | 33.8 | 1.8 |
| Mnz-2-09 | 312 | 1001 | 3.2 | 1.1857 | 3.97 | 0.0064 | 1.65 | 0.1776 | 4.09 | 17 | 29 | 34.2 | 0.8 | 34.1 | 1.1 |
| Mnz-3-01 | 174 | 391 | 2.2 | 1.2230 | 3.82 | 0.0095 | 3.13 | 0.3385 | 4.05 | 37 | 62 | 38.6 | 2.2 | 38.0 | 1.4 |
| Mnz-3-02 | 135 | 23 | 0.2 | 0.6603 | 5.70 | 0.0087 | 3.82 | 0.2895 | 5.63 | 31 | 96 | 38.8 | 2.2 | 15.9 | 0.9 |
| Mnz-3-03 | 207 | 339 | 1.6 | 0.7910 | 10.43 | 0.0058 | 3.15 | 0.1373 | 3.84 | 11 | 30 | 32.8 | 1.1 | 38.2 | 2.4 |
| Mnz-4-01 | 169 | 1510 | 8.9 | 2.6121 | 3.98 | 0.0102 | 5.54 | 0.2991 | 6.59 | 32 | 25 | 44.5 | 3.2 | 36.4 | 1.1 |
| Mnz-4-02 | 35 | 2561 | 73.2 | 6.7809 | 3.39 | 0.0259 | 3.55 | 0.6236 | 5.18 | 73 | 22 | 44.7 | 10.4 | 38.5 | 0.9 |
| Mnz-4-03 | 97 | 2293 | 23.7 | 5.7482 | 3.81 | 0.0073 | 3.37 | 0.1922 | 10.68 | 18 | 7 | 38.5 | 1.9 | 34.9 | 0.8 |
| Mnz-4-04 | 140 | 2400 | 17.2 | 4.3563 | 5.21 | 0.0092 | 3.30 | 0.3305 | 6.19 | 36 | 17 | 37.9 | 2.4 | 39.5 | 1.1 |
| Mnz-5-01 | 101 | 3903 | 38.6 | 6.0357 | 2.89 | 0.0155 | 2.55 | 0.5719 | 4.09 | 66 | 23 | 33.3 | 5.2 | 35.2 | 0.6 |

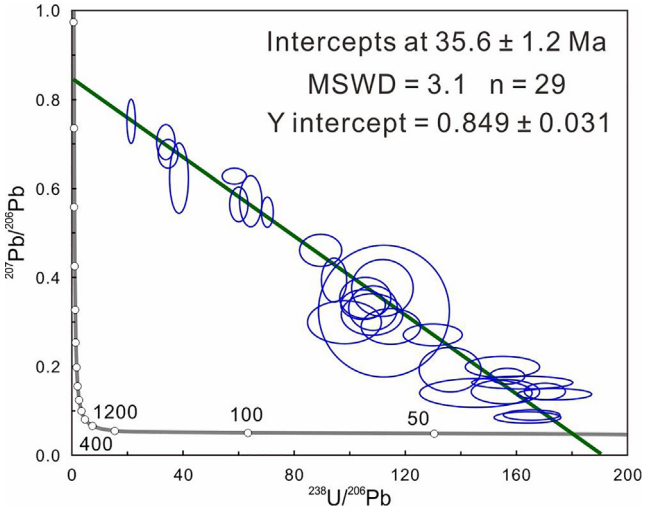


**Fig. 8.** Tera-Wasserburg U–Pb plot for the hydrothermal monazite from the Beiya gold deposit.

U and thus, $^{230}$Th, an intermediate product of the $^{238}$U decay chain (with a half-life of 75.4 ky) is preferentially partitioned into the monazite structure over its parent $^{238}$U isotope (Schärer, 1984; Schoene, 2014). The decay of $^{230}$Th is responsible for excess $^{206}$Pb of monazite. For the hydrothermal monazite at Beiya, there is a mild positive correlation between Th/U ratio and $^{206}$Pb/$^{238}$U age, especially for grains with Th/U ratios exceeding 10 (Fig. 11). This demonstrates the probable effect of excess $^{206}$Pb on $^{206}$Pb/$^{238}$U ages. Therefore, we propose that the weighted mean corrected $^{208}$Pb/$^{232}$Th age of 36.0 ± 0.5 Ma is the most reliable result, representing the formation age of hydrothermal monazite from the Beiya gold deposit.

### 5.3. Comparison with other ages

Previous attempts of dating the Beiya gold mineralization were based on molybdenite, sphalerite, titanite and allanite, which are summarized in Table 5 (references therein). These results, however, should be interpreted in caution for several reasons. Firstly, the dated minerals including molybdenite, titanite and allanite occur in skarn samples which are largely dominated by garnet and diopside. Such samples differ from typical massive gold ores that mainly consist of magnetite and sulfide minerals. Also, the localities for the dated minerals and gold are different at Beiya. Specifically, those samples containing molybdenite were collected from the Hongnitang sector alone or are mixed from Hongnitang and Wandongshan (e.g., He et al., 2013, 2015; Liu, 2014; Fu et al., 2015; Niu et al., 2015), yet gold is hosted by Wandongshan for the most part. Therefore, the molybdenite Re-Os isochron ages (38.1–34.7 Ma) may not correspond to the gold deposition although the molybdenite results have been widely regarded as the best ages for the Beiya gold mineralization (He et al., 2013; Fu et al., 2015; He et al., 2015; Niu et al., 2015).

Secondly, the reported ages of titanite and allanite were based on the non matrix-matched U-Pb dating methods via LA-ICP-MS (static) spot ablation in these studies (Fu et al., 2016, 2017). A bias caused by matrix effect related to different fractionation behavior of U/Pb and Th/Pb isotopes in titanite, allanite, and the non matrix-matched standards (e.g., zircon) has been recorded in published literature (e.g., Darling et al., 2012; Sun et al., 2012). Thus, we suggest that the titanite ages should be considered as less-robust chronological constraints on the gold mineralization.

Thirdly, the recently reported sphalerite age represents material from the Pb-Zn-Ag ores in the Bijiashan segment (Wang, 2017). Its (Rb-Sr) chronological result (32.8 ± 1.9 Ma; Wang, 2017), provides a useful constraint on the Pb-Zn-Ag mineralization, but may not be directly relevant for the timing of the Beiya gold mineralization.

The monazite grains used in this study were carefully selected from

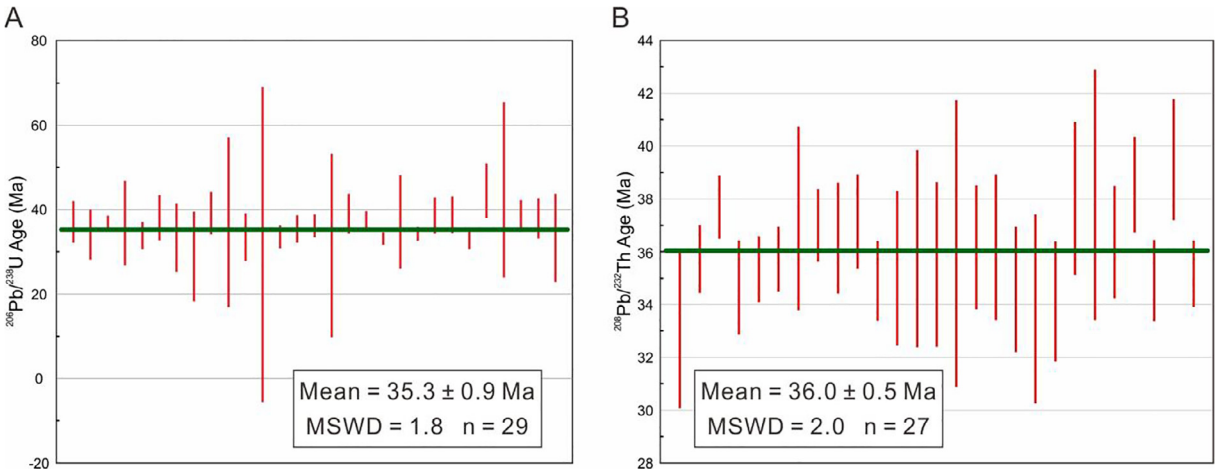


**Fig. 9.** Wight mean of $^{206}Pb/^{238}U$ (A) and $^{208}Pb/^{232}Th$ (B) ages for the hydrothermal monazite from the Beiya gold deposit.

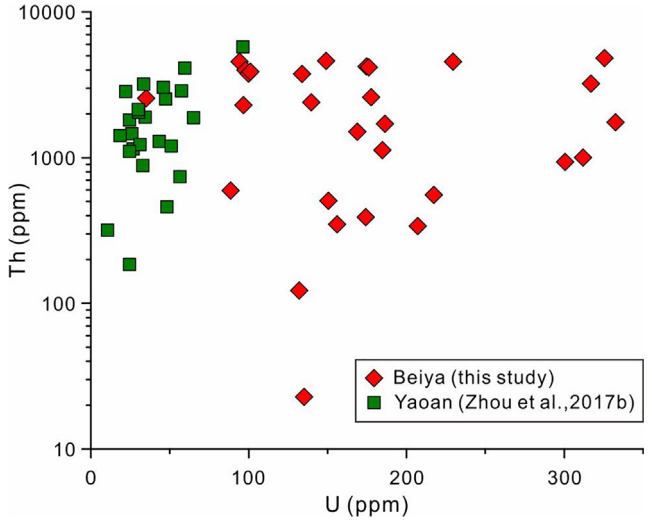


**Fig. 10.** Scatter plot of U versus Th concentrations in the hydrothermal monazite both from the Beiya and Yaoan gold deposits.

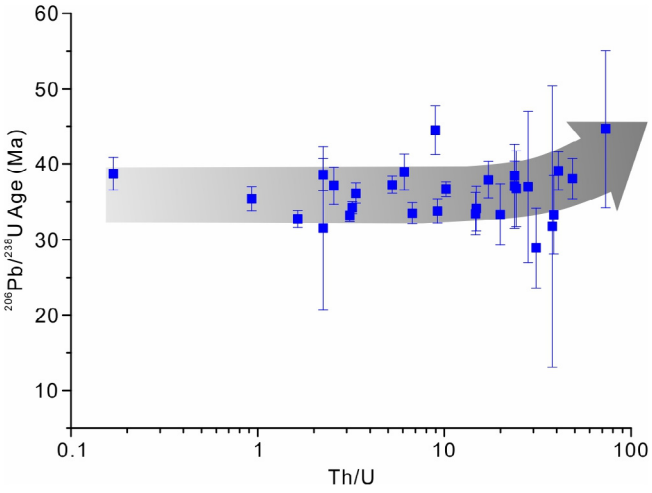


**Fig. 11.** Plot of Th/U ratio versus $^{206}Pb/^{238}U$ age illustrating the influence of excess $^{206}Pb$.

the high-grade gold ore samples at Wandongshan, which are characterized by a typical assemblage of magnetite, pyrite and chalcopyrite. In addition, there are direct associations between monazite and these ore minerals (magnetite, pyrite and chalcopyrite), which have been recognized as important gold carriers at Beiya (Zhou et al., 2016, 2017a). We thus suggest that the crystallization of monazite is coeval with skarn gold deposition and our monazite geochronological result is therefore a reliable age for the Beiya skarn gold mineralization. This age can also be regarded as the time of skarn iron mineralization.

### 5.4. Implications for Beiya skarn gold mineralization

The Beiya quartz monzonite porphyry has been dated by many studies using zircon U-Pb isotopes, the results of which are summarized in Table 6 (references therein). Available zircon ages of the quartz monzonite porphyry at Wandongshan are in the range between 37.9 and 34.7 Ma. The zircon crystals from the Wandongshan quartz monzonite porphyry dated in this study are mostly euhedral with oscillatory CL zoning and Th/U > 0.5, suggestive of a magmatic origin (e.g., Hoskin and Schaltegger, 2003; Wu and Zheng, 2004). Within uncertainty, our new zircon age (37.2 ± 0.4 Ma) is in good agreement with the previous age range. The published zircon ages for the quartz monzonite porphyry at Hongnitang range from 36.6 to 36.1 Ma, which is in the same range as for Wandongshan.

Alkaline intrusions were emplaced in the southern part of the Jinshajiang-Red River belt during 37–32 Ma (Lu et al., 2012). Our new zircon data and previously-reported ages suggest that the Beiya quartz monzonite magmatism is contemporaneous with the regional alkaline magmatism. Based on the whole-rock trace element geochemistry and Sr-Nd-Pb isotopes, as well as zircon Hf-O isotopes, it has been suggested that melting of the subcontinental lithospheric mantle resulted in partial melting of a thickened and K-rich mafic lower crust, which formed the source of the Beiya alkaline granitic intrusions (Lu et al., 2013; Deng et al., 2015a).

This study shows that the skarn gold mineralization, dated by hydrothermal monazite at 36.0 ± 0.5 Ma, is coeval with the quartz monzonite magmatism at Beiya. Given that sulfide minerals (e.g., pyrite and chalcopyrite) from the skarn gold ores display S isotopes suggestive of magmatic origin and have Pb isotope composition similar to the quartz monzonite porphyry (He et al., 2017), our geochronological results confirm a genetic link between the Beiya skarn gold mineralization and the quartz monzonite magmatism. The monazite age also favors the view that skarn gold deposition is contemporaneous with the skarn molybdenite, but older than the Bijiashan Pb-Zn-Ag mineralization. The latter is reasonable considering that this mineralization is distal to the quartz monzonite porphyry, and formed at lower temperature. Fluid inclusions in quartz coexisting with the gold-bearing assemblage (e.g., magnetite, pyrite and chalcopyrite) in skarn gold ores yielded homogenization temperatures up to 538 °C (He et al., 2017),

**Table 5**
Reported ages for the Beiya mineralization.

| Dating method (isotope external standard) | Sample location | Age (2σ; Ma) | Source |
|---|---|---|---|
| Molybdenite Re-Os | Wandongshan and Hongnitang | 36.82 ± 0.48 | He et al. (2015) |
| | | 37.9 ± 2.5 | Niu et al. (2015) |
| | | 38.12 ± 0.82 | Liu (2014) |
| | Hongnitang | 36.87 ± 0.76 | He et al. (2013) |
| | | 34.7 ± 1.6 | Fu et al. (2015) |
| Titanite U-Pb (zircon) | Wandongshan | 33.1 ± 1.0 | Fu et al. (2016) |
| Allanite Th-Pb (zircon) | Wandongshan | 33.4 ± 4.6 | Fu et al. (2017) |
| Monazite Th-Pb (monazite) | Wandongshan | 36.0 ± 0.5 | This study |
| Sphalerite Rb-Sr | Bijiashan | 32.8 ± 1.9 | Wang (2017) |

**Table 6**
Reported weight mean $^{206}Pb/^{238}U$ ages of zircon from the quartz monzonite porphyry at Beiya.

| Location | Method | Age (2σ; Ma) | Source |
|---|---|---|---|
| Wandongshan | SHRIMP | 36.9 ± 0.3 | Lu et al. (2012) |
| | | 37.9 ± 0.8 | Hou et al. (2017) |
| | LA-MC-ICP-MS | 36.2 ± 0.7 | Bao et al. (2017) |
| | LA-ICP-MS | 34.9 ± 0.7 | He et al. (2012) |
| | | 36.5 ± 1.1 | Jiang et al. (2013) |
| | | 34.7 ± 0.8 | Deng et al. (2015a) |
| | | 34.7 ± 0.9 | |
| | | 35.4 ± 0.6 | |
| | | 35.7 ± 0.6 | |
| | | 35.9 ± 0.6 | |
| | | 36.3 ± 0.7 | |
| | | 36.6 ± 0.7 | |
| | | 36.2 ± 0.1 | He et al. (2015) |
| | | 35.0 ± 1.0 | Liu et al. (2015) |
| | | 36.3 ± 0.1 | He et al. (2016a) |
| | | 36.7 ± 0.2 | |
| | | 36.7 ± 0.3 | |
| | | 37.2 ± 0.4 | This study |
| Hongnitang | SHRIMP | 36.2 ± 0.3 | Lu et al. (2012) |
| | LA-ICP-MS | 36.2 ± 0.6 | He et al. (2012) |
| | | 36.5 ± 0.3 | He et al. (2013) |
| | | 36.1 ± 0.4 | Fu et al. (2015) |
| | | 35.1 ± 0.2 | Liu et al. (2015) |
| | | 36.6 ± 0.4 | He et al. (2016a) |

whereas those in calcite and quartz from the Bijiashan Pb-Zn-Ag ores are 242–340 °C (Wang et al., 2015).

Our study demonstrates that judicious selection of mineralization-related geochronometers is essential for determining the timing of mineralization in giant polymetallic mineral systems. For skarn systems, we suggest that monazite can be a robust chronometer, especially for gold subtypes, in addition to the more commonly-used sulfide minerals (e.g., pyrrhotite and molybdenite; Wang et al., 2008; Chiaradia et al., 2009), hydrous silicates (e.g., muscovite, biotite and phlogopite; Xie et al., 2012), and accessory phases (e.g., zircon and titanite; Deng et al., 2015b; Zhao et al., 2016; Lawrence et al., 2017).

## 6. Conclusions

Hydrothermal monazite co-precipitated with gold-hosting ore minerals (e.g., magnetite, pyrite and chalcopyrite) was identified in the high-grade skarn gold ores from the world-class Beiya polymetallic gold deposit. In situ SIMS U-Th-Pb dating of monazite reveals variable fractions of common Pb and the influence of excess $^{206}Pb$. Taking this into account, the $^{208}Pb/^{232}Th$ age of 36.0 ± 0.5 Ma (2σ, MSWD = 2.0, n = 27) for hydrothermal monazite is interpreted as a robust age for the Beiya skarn gold deposition. The new age implies that skarn gold mineralization is probably synchronous with the formation of skarn molybdenite, but older than local Pb-Zn-Ag mineralization. A new U-Pb zircon age for the associated quartz monzonite porphyry intrusion (37.2 ± 0.4 Ma) agrees with previous work and supports a genetic relationship with the Beiya skarn gold mineralization.

## Acknowledgements

This work was jointly supported by the National Natural Science Foundation of China (Nos. 91855213, U1302233, 41672071, 40830425, 40673045), the National Key Basic Research Program (Nos. 2015CB452604, 2009CB421006), the Higher School Specialized Research Fund for the Doctoral Program Funding Issue (No. 200805580031), the Pearl River Scholar Funded Scheme (2011), and the Sino-German (CSC-DAAD) Postdoc Scholarship Program to H.Y. Zhou. The authors thank Xianhua Li and Xiaoxiao Ling for their support in the SIMS analysis. Robert Trumbull is thanked for language polishing. This manuscript benefits from critical comments from two anonymous reviewers.

## References

Aleinikoff, J.N., Schenck, W.S., Plank, M.O., Srogi, L., Fanning, C.M., Kamo, S.L., Bosbyshell, H., 2006. Deciphering igneous and metamorphic events in high-grade rocks of the Wilmington Complex, Delaware: Morphology, cathodoluminescence and backscattered electron zoning, and SHRIMP U-Pb geochronology of zircon and monazite. Geol. Soc. Am. Bull. 118, 39–64.

Arehart, G.B., Chakurian, A.M., Tretbar, D.R., Christensen, J.N., McInnes, B.A., Donelick, R.A., 2003. Evaluation of radioisotope dating of Carlin-type deposits in the Great Basin, western North America, and implications for deposit genesis. Econ. Geol. 98, 235–248.

Bao, X.S., He, W.Y., Gao, X., 2017. The Beiya gold deposit: Constraint from water-rich magmas to mineralization. Acta Petrol. Sin. 33, 2175–2188 (in Chinese with English abstract).

Bosse, V., Boulvais, P., Gautier, P., Tiepolo, M., Ruffet, G., Devidal, J.L., Cherneva, Z., Gerdjikov, I., Paquette, J.L., 2009. Fluid-induced disturbance of the monazite Th–Pb chronometer: in situ dating and element mapping in pegmatites from the Rhodope (Greece, Bulgaria). Chem. Geol. 261, 286–302.

Chiaradia, M., Vallance, J., Fontboté, L., Stein, H., Schaltegger, U., Coder, J., Richards, J., Villeneuve, M., Gendall, I., 2009. U-Pb, Re–Os, and $^{40}Ar/^{39}Ar$ geochronology of the Nambija Au-skarn and Pangui porphyry Cu deposits, Ecuador: implications for the Jurassic metallogenic belt of the Northern Andes. Miner. Deposita 44, 371–387.

Chung, S.L., Lee, T.Y., Lo, C.H., Wang, P.L., Chen, C.Y., Yem, N.T., Hoa, T.T., Genyao, W., 1997. Intraplate extension prior to continental extrusion along the Ailao Shan-Red River shear zone. Geology 25, 311–314.

Chung, S.L., Lo, C.H., Lee, T.Y., Zhang, Y.Q., Xie, Y.W., Li, X.H., Wang, K.L., Wang, P.L., 1998. Diachronous uplift of the Tibetan plateau starting 40 Myr ago. Nature 394, 769–773.

Darling, J.R., Storey, C.D., Engi, M., 2012. Allanite U-Th–Pb geochronology by laser ablation ICPMS. Chem. Geol. 292, 103–115.

Deng, J., Wang, Q.F., Li, G.J., Santosh, M., 2014. Cenozoic tectono-magmatic and metallogenic processes in the Sanjiang region, southwestern China. Earth Sci. Rev. 138, 268–299.

Deng, J., Wang, Q.F., Li, G.J., Hou, Z.Q., Jiang, C.Z., Danyushevsky, L., 2015a. Geology and genesis of the giant Beiya porphyry–skarn gold deposit, northwestern Yangtze Block, China. Ore Geol. Rev. 70, 457–485.

Deng, X.D., Li, J.W., Wen, G., 2015b. U-Pb geochronology of hydrothermal zircons from the early Cretaceous iron skarn deposits in the Handan-Xingtai district, North China craton. Econ. Geol. 110, 2159–2180.

Fielding, I.O.H., Johnson, S.P., Zi, J.W., Rasmussen, B., Muhling, J.R., Dunkley, D.J., Sheppard, S., Wingate, M.T.D., Rogers, J.R., 2017. Using in situ SHRIMP U-Pb monazite and xenotime geochronology to determine the age of orogenic gold mineralization: an example from the Paulsens Mine, southern Pilbara Craton. Econ. Geol. 112, 1205–1230.

Fletcher, I.R., McNaughton, N.J., Davis, W.J., Rasmussen, B., 2010. Matrix effects and calibration limitations in ion probe U-Pb and Th–Pb dating of monazite. Chem. Geol.

270, 31–44.
Fu, Y., Sun, X.M., Lin, H., Zhou, H.Y., Li, X., Ouyang, X.Q., Jiang, L.Y., Shi, G.Y., Liang, Y.H., 2015. Geochronology of the giant Beiya gold-polymetallic deposit in Yunnan Province, Southwest China and its relationship with the petrogenesis of alkaline porphyry. Ore Geol. Rev. 71, 138–149.
Fu, Y., Sun, X.M., Zhou, H.Y., Lin, H., Yang, T.J., 2016. In-situ LA–ICP–MS U-Pb geochronology and trace elements analysis of polygenetic titanite from the giant Beiya gold–polymetallic deposit in Yunnan Province, Southwest China. Ore Geol. Rev. 77, 43–56.
Fu, Y., Sun, X.M., Li, D.F., Lin, H., Lai, C., 2017. LA-ICP-MS U-Th-Pb dating and trace element geochemistry of allanite: implications on the different skarn metallogenesis between the giant Beiya Au and Machangqing Cu-Mo-(Au) deposits in Yunnan, SW China. Minerals 7, 251.
Harlan, S.S., Vielreicher, R.M., Mortensen, J.M., Bradley, D.C., Goldfarb, R.J., Snee, L.W., Till, A.B., 2017. Geology and timing of ore formation in the Willow Creek gold district, Talkeetna Mountains, southern Alaska. Econ. Geol. 112, 1177–1204.
He, W.Y., Yu, X.H., Mo, X.X., He, Z.H., Li, Y., Huang, X.K., Su, G.S., 2012. Genetic types and the relationship between alkali-rich intrusion and mineralization of Beiya gold-polymetallic ore field, western Yunnan Province, China. Acta Petrol. Sin. 28, 1401–1412 (in Chinese with English abstract).
He, W.Y., Mo, X.X., Yu, X.H., He, Z.H., Dong, G.C., Liu, X.B., Su, G.S., Huang, X.F., 2013. Zircon U-Pb and molybdenite Re-Os dating for the Beiya gold-polymetallic deposit in the western Yunnan Province and its geological significance. Acta Petrol. Sin. 29, 1301–1310 (in Chinese with English abstract).
He, W.Y., Mo, X.X., He, Z.H., White, N.C., Chen, J.B., Yang, K.H., Wang, R., Yu, X.H., Dong, G.C., Huang, X.F., 2015. The geology and mineralogy of the Beiya skarn gold deposit in Yunnan, Southwest China. Econ. Geol. 110, 1625–1641.
He, W.Y., Mo, X.X., Yang, L.Q., Xing, Y.L., Dong, G.C., Yang, Z., Gao, X., Bao, X.S., 2016a. Origin of the Eocene porphyries and mafic microgranular enclaves from the Beiya porphyry Au polymetallic deposit, western Yunnan, China: implications for magma mixing/mingling and mineralization. Gondwana Res. 40, 230–248.
He, W.Y., Yang, L.Q., Brugger, J., McCuaig, T.C., Lu, Y.J., Bao, X.S., Gao, X.Q., Lu, Y.G., Xing, Y.L., 2017. Hydrothermal evolution and ore genesis of the Beiya giant Au polymetallic deposit, western Yunnan, China: evidence from fluid inclusions and H-O-S-Pb isotopes. Ore Geol. Rev. 90, 847–862.
He, Z.H., Guan, D.R., He, W.Y., Zhou, Y.M., Fu, D.G., Yang, S.W., Lu, Y.Z., Wang, L.D., Li, W.H., Su, G.S., Yang, R., 2016b. Exploration model of Beiya superlarge gold-polymetallic deposit, northwestern Yunnan. Miner. Deposits 35, 261–282 (in Chinese with English abstract).
Hoskin, P.W.O., Schaltegger, U., 2003. The composition of zircon and igneous and metamorphic petrogenesis. Rev. Miner. Geochem. 53, 27–62.
Hou, Z.Q., Zhong, D.L., Deng, W.M., 2004. A tectonic model for porphyry copper-molybdenum-gold metallogenic belts on the eastern margin of the Qinghai-Tibet Plateau. Geol. China 31, 1–14 (in Chinese with English abstract).
Hou, Z.Q., Zeng, P.S., Gao, Y.F., Du, A.D., Fu, D.M., 2006. Himalayan Cu–Mo–Au mineralization in the eastern Indo-Asian collision zone: constraints from Re–Os dating of molybdenite. Miner. Deposita 41, 33–45.
Hou, Z.Q., Zhou, Y., Wang, R., Zheng, Y.C., He, W.Y., Zhao, M., Evans, N.J., Weinberg, R.F., 2017. Recycling of metal-fertilized lower continental crust: origin of non-arc Au-rich porphyry deposits at cratonic edges. Geology 45, 563–566.
Janots, E., Berger, A., Gnos, E., Whitehouse, M., Lewin, E., Pettke, T., 2012. Constraints on fluid evolution during metamorphism from U-Th–Pb systematics in Alpine hydrothermal monazite. Chem. Geol. 326–327, 61–71.
Jiang, C.Z., Wang, Q.F., Li, G.J., Ma, N., Hu, Z.C., 2013. Relative oxidation states of intrusions in Beiya gold-polymetallic deposit in Sanjiang area, Yunnan, SW China. Acta Petrol. Sin. 29, 3925–3936 (in Chinese with English abstract).
Kempe, U., Lehmann, B., Wolf, D., Rodionov, N., Bombach, K., Schwengfelder, U., Dietrich, A., 2008. U-Pb SHRIMP geochronology of Th-poor, hydrothermal monazite: an example from the Llallagua tin-porphyry deposit, Bolivia. Geochim. Cosmochim. Acta 72, 4352–4366.
Kirk, J., Ruiz, J., Chesley, J., Walshe, J., England, G., 2002. A major Archean, gold-and crust-forming event in the Kaapvaal Craton, South Africa. Science 297, 1856–1858.
Lawrence, D.M., Allibone, A.H., Chang, Z., Meffre, S., Lambert-Smith, J.S., Treloar, P.J., 2017. The Tongon Au deposit, northern Côte d'Ivoire: an example of Paleoproterozoic Au skarn mineralization. Econ. Geol. 112, 1571–1593.
Li, Q.L., Li, X.H., Lan, Z.W., Guo, C.L., Yang, Y.N., Liu, Y., Tang, G.Q., 2013. Monazite and xenotime U-Th–Pb geochronology by ion microprobe: dating highly fractionated granites at Xihuashan tungsten mine, SE China. Contrib. Miner. Petrol. 166, 65–80.
Li, W.C., Wang, J.H., He, Z.H., Dou, S., 2016. Formation of Au-polymetallic ore deposits in alkaline porphyries at Beiya, Yunnan, Southwest China. Ore Geol. Rev. 73, 241–252.
Liang, H.Y., Sun, W.D., Su, W.C., Zartman, R.E., 2009. Porphyry copper-gold mineralization at Yulong, China, promoted by decreasing redox potential during magnetite alteration. Econ. Geol. 104, 587–596.
Ling, X.X., Huyskens, M.H., Li, Q.L., Yin, Q.Z., Werner, R., Liu, Y., Tang, G.Q., Yang, Y.N., Li, X.H., 2017. Monazite RW-1: a homogenous natural reference material for SIMS U-Pb and Th–Pb isotopic analysis. Miner. Petrol. 111, 163–172.
Liu, B., 2014. Geological Features of Diagenesis and Mineralization in the Beiya Gold Polymetallic Deposit, Western Yunnan Province (M.S.D. thesis). China University of Geosciences, Beijing, pp. 52–55 (in Chinese with English abstract).
Liu, B., Liu, H., Zhang, C.Q., Mao, Z.H., Zhou, Y.M., Huang, H., He, Z.H., Su, G.S., 2015. Geochemistry and geochronology of porphyries from the Beiya gold–polymetallic orefield, western Yunnan, China. Ore Geol. Rev. 69, 360–379.
Liu, Y.S., Gao, S., Hu, Z.C., Gao, C.G., Zong, K.Q., Wang, D.B., 2010. Continental and oceanic crust recycling-induced melt–peridotite interactions in the Trans-North China Orogen: U-Pb dating, Hf isotopes and trace elements in zircons from mantle xenoliths. J. Petrol. 51, 537–571.
Lu, Y.J., Kerrich, R., Cawood, P.A., McCuaig, T.C., Hart, C.J.R., Li, Z.X., Hou, Z.Q., Bagas, L., 2012. Zircon SHRIMP U-Pb geochronology of potassic felsic intrusions in western Yunnan, SW China: constraints on the relationship of magmatism to the Jinsha suture. Gondwana Res. 22, 737–747.
Lu, Y.J., Kerrich, R., Mccuaig, T.C., Li, Z.X., Hart, C.J.R., Cawood, P.A., Hou, Z.Q., Bagas, L., Cliff, J., Belousova, E.A., Tang, S.H., 2013. Geochemical, Sr–Nd–Pb, and zircon Hf–O isotopic compositions of Eocene-Oligocene shoshonitic and potassic adakite-like felsic intrusions in western Yunnan, SW China: petrogenesis and tectonic implications. J. Petrol. 54, 1309–1348.
Ludwig, K.R., 2003. User's Manual for Isoplot 3.00: A Geochronological Toolkit for Microsoft Excel. Berkeley Chronology Center Special Publication 4, pp. 1–75.
Mao, J.W., Zhou, Y.M., Liu, H., Zhang, C.Q., Fu, D.G., Liu, B., 2017. Metallogenic setting and ore genetic model for the Beiya porphyry-skarn polymetallic Au orefield, western Yunnan, China. Ore Geol. Rev. 86, 21–34.
Meffre, S., Large, R.R., Steadman, J.A., Gregory, D.D., Stepanov, A.S., Kamenetsky, V.S., Ehrig, K., Scott, R.J., 2016. Multi-stage enrichment processes for large gold-bearing ore deposits. Ore Geol. Rev. 76, 268–279.
Morelli, R., Creaser, R.A., Seltmann, R., Stuart, F.M., Selby, D., Graupner, T., 2007. Age and source constraints for the giant Muruntau gold deposit, Uzbekistan, from coupled Re-Os-He isotopes in arsenopyrite. Geology 35, 795–798.
Niu, H.B., Hu, W.Y., Ding, J., Li, J., Ning, K.B., Wang, P., Ren, F., Dong, L.Y., 2015. Re-Os isotope age of Molybdenite in the Beiya Au-polymetallic deposit, Western Yunnan Province and its geological implications. Geol. Explor. 51, 1–12 (in Chinese with English abstract).
Parrish, R.R., 1990. U-Pb dating of monazite and its application to geological problems. Can. J. Earth Sci. 27, 1431–1450.
Pelleter, E., Cheilletz, A., Gasquet, D., Mouttaqi, A., Annich, M., El Hakour, A., Deloule, E., Féraud, G., 2007. Hydrothermal zircons: a tool for ion microprobe U-Pb dating of gold mineralization (Tamlalt–Menhouhou gold deposit — Morocco). Chem. Geol. 245, 135–161.
Rasmussen, B., Sheppard, S., Fletcher, I.R., 2006. Testing ore deposit models using in situ U-Pb geochronology of hydrothermal monazite: Paleoproterozoic gold mineralization in northern Australia. Geology 34, 77–80.
Rasmussen, B., Fletcher, I.R., Muhling, J.R., Mueller, A.G., Hall, G.C., 2007a. Bushveld-aged fluid flow, peak metamorphism, and gold mobilization in the Witwatersrand basin, South Africa: constraints from in situ SHRIMP U-Pb dating of monazite and xenotime. Geology 35, 931–934.
Rasmussen, B., Fletcher, I.R., Muhling, J.R., Thorne, W.S., Broadbent, G.C., 2007b. Prolonged history of episodic fluid flow in giant hematite ore bodies: evidence from in situ U-Pb geochronology of hydrothermal xenotime. Earth Planet. Sci. Lett. 258, 249–259.
Rasmussen, B., Zi, J., Sheppard, S., Krapež, B., Muhling, J.R., 2016. Multiple episodes of hematite mineralization indicated by U-Pb dating of iron-ore deposits, Marquette Range, Michigan, USA. Geology 44, 547–550.
Sarma, D.S., Mcnaughton, N.J., Fletcher, I.R., Groves, D.I., Ram Mohan, M., Balaram, V., 2008. Timing of gold mineralization in the Hutti gold deposit, Dharwar Craton, South India. Econ. Geol. 103, 1715–1727.
Sarma, D.S., Fletcher, I.R., Rasmussen, B., McNaughton, N.J., Mohan, M.R., Groves, D.I., 2011. Archaean gold mineralization synchronous with late cratonization of the Western Dharwar Craton, India: 2.52 Ga U-Pb ages of hydrothermal monazite and xenotime in gold deposits. Miner. Deposita 46, 273–288.
Schandl, E.S., Gorton, M.P., 2004. A textural and geochemical guide to the identification of hydrothermal monazite: criteria for selection of samples for dating epigenetic hydrothermal ore deposits. Econ. Geol. 99, 1027–1035.
Schärer, U., 1984. The effect of initial $^{230}$Th disequilibrium on young U-Pb ages: the Makalu case, Himalaya. Earth Planet. Sci. Lett. 67, 191–204.
Schärer, U., Tapponnier, P., Lacassin, R., Leloup, P.H., Zhong, D.L., Ji, S.C., 1990. Intraplate tectonics in Asia: a precise age for large-scale Miocene movement along the Ailao Shan-Red River shear zone, China. Earth Planet. Sci. Lett. 97, 65–77.
Schoene, B., 2014. U-Th–Pb geochronology. In: Holland, H., Turekian, K. (Eds.), Treatise on Geochemistry, second ed. Elsevier, Amsterdam, pp. 341–378.
Schulze, D.J., Davis, D.W., Helmstaedt, H., Joy, B., 2015. Timing of the Cenozoic "Great Hydration" event beneath the Colorado Plateau: Th-Pb dating of monazite in Navajo volcanic field metamorphic eclogite xenoliths. Geology 43, 727–730.
Selby, D., Creaser, R.A., Hart, C.J.R., Rombach, C.S., Thompson, J.F.H., Smith, M.T., Bakke, A.A., Goldfarb, R.J., 2002. Absolute timing of sulfide and gold mineralization: a comparison of Re-Os molybdenite and Ar-Ar mica methods from the Tintina Gold Belt, Alaska. Geology 30, 791–794.
Sláma, J., Košler, J., Condon, D.J., Crowley, J.L., Gerdes, A., Hanchar, J.M., Horstwood, M.S.A., Morris, G.A., Nasdala, L., Norberg, N., Schaltegger, U., Schoene, B., Tubrett, M.N., Whitehouse, M.J., 2008. Plešovice zircon – a new natural reference material for U-Pb and Hf isotopic microanalysis. Chem. Geol. 249, 1–35.
Stacey, J.S., Kramers, J.D., 1975. Approximation of terrestrial lead isotope evolution by a two-stage model. Earth Planet. Sci. Lett. 26, 207–221.
Sun, J.F., Yang, J.H., Wu, F.Y., Xie, L.W., Yang, Y.H., Liu, Z.C., Li, X.H., 2012. In situ U-Pb dating of titanite by LA-ICPMS. Chin. Sci. Bull. 57, 2506–2516.
Tapponnier, P., Lacassin, R., Leloup, P.H., Scharer, U., Zhong, D.L., Wu, H.W., Liu, X.H., Ji, S.C., Zhang, L.S., Zhong, J.Y., 1990. The Ailao Shan/Red River metamorphic belt: tertiary left-lateral shear between Indochina and South China. Nature 343, 431–437.
Tretbar, D.R., Arehart, G.B., Christensen, J.N., 2000. Dating gold deposition in a Carlin-type gold deposit using Rb/Sr methods on the mineral galkhaite. Geology 28, 947–950.
Turner, S., Arnaud, N., Liu, J., Rogers, N., Hawkesworth, C., Harris, N., Kelley, S., Van Calsteren, P., Deng, W., 1996. Post-collision, shoshonitic volcanism on the Tibetan Plateau: implications for convective thinning of the lithosphere and the source of

ocean island basalts. J. Petrol. 37, 45–71.
van Emden, B., Thornber, M.R., Graham, J., Lincoln, F.J., 1997. The incorporation of actinides in monazite and xenotime from placer deposits in Western Australia. Can. Miner. 35, 95–104.
Wang, J.H., Yin, A., Harrison, T.M., Grove, M., Zhang, Y.Q., Xie, G.H., 2001. A tectonic model for Cenozoic igneous activities in the eastern Indo-Asian collision zone. Earth Planet. Sci. Lett. 188, 123–133.
Wang, J.H., Li, W.C., Wang, K.Y., Yin, G.H., Wu, S., Jiang, W.T., 2015. The characteristics and evolution of the ore-forming fluids in the Beiya porphyry Au-polymetallic deposit, western Yunnan. Acta Petrol. Sin. 31, 3269–3280 (in Chinese with English abstract).
Wang, J.H., 2017. Alkaline-rich Porphyry Au-polymetallic Metallogeny System in Beiya, Heqing, west Yunnan (Ph.D. thesis). Kunming University of Science and Technology, Kunming, pp. 102–106 (in Chinese with English abstract).
Wang, J.Z., Li, J.W., Zhao, X.F., Ma, C.Q., Qu, W.J., Du, A.D., 2008. Re-Os dating of pyrrhotite from the Chaoshan gold skarn, eastern Yangtze Craton, eastern China. Int. Geol. Rev. 50, 392–406.
Wang, X.F., Metcalfe, I., Jian, P., He, L.Q., Wang, C.S., 2000. The Jinshajiang-Ailaoshan Suture Zone, China: tectonostratigraphy, age and evolution. J. Asian Earth Sci. 18, 675–690.
Westhues, A., Hanchar, J.M., Whitehouse, M.J., Martinsson, O., 2016. New constraints on the timing of host-rock emplacement, hydrothermal alteration, and iron oxide-apatite mineralization in the Kiruna district, Norrbotten, Sweden. Econ. Geol. 111, 1595–1618.
Williams, I.S., 1998. U-Th-Pb geochronology by ion microprobe. Rev. Econ. Geol. 17, 1–35.
Wu, Y.B., Zheng, Y.F., 2004. Genesis of zircon and its constraints on interpretation of U-Pb age. Chin. Sci. Bull. 49, 1554–1569.
Xie, G.Q., Mao, J.W., Zhao, H.J., Duan, C., Yao, L., 2012. Zircon U-Pb and phlogopite $^{40}Ar$-$^{39}Ar$ age of the Chengchao and Jinshandian skarn Fe deposits, southeast Hubei Province, Middle-Lower Yangtze River Valley metallogenic belt, China. Miner. Deposita 47, 633–652.
Yin, A., Harrison, T.M., 2000. Geologic evolution of the Himalayan-Tibetan orogen. Annu. Rev. Earth Planet. Sci. 28, 211–280.
Yunnan Gold & Mineral Group Co., Ltd, 2013. Reserves Verification Report of the Beiya Iron-gold Deposit, Heqing, Yunnan Province. Yunnan Gold & Mineral Group Co., Ltd, Kunming (in Chinese).
Zhao, W.W., Zhou, M.F., Chen, W.T., 2016. Growth of hydrothermal baddeleyite and zircon in different stages of skarnization. Am. Miner. 101, 2689–2700.
Zhou, H.Y., Sun, X.M., Fu, Y., Lin, H., Jiang, L.Y., 2016. Mineralogy and mineral chemistry of Bi-minerals: constraints on ore genesis of the Beiya giant porphyry-skarn gold deposit, southwestern China. Ore Geol. Rev. 79, 408–424.
Zhou, H.Y., Sun, X.M., Cook, N.J., Lin, H., Fu, Y., Zhong, R.C., Brugger, J., 2017a. Nano- to micron-scale particulate gold hosted by magnetite: a product of gold scavenging by bismuth melts. Econ. Geol. 112, 993–1010.
Zhou, H.Y., Sun, X.M., Wu, Z.W., Liao, J.L., Fu, Y., Li, D., Pete, H., Liu, Y., Lin, H., Lin, Z.Y., 2017b. Hematite U-Pb geochronometer: insights from monazite and hematite integrated chronology of the Yaoan gold deposit, southwest China. Econ. Geol. 112, 2023–2039.
Zhou, H.Y., Sun, X.M., Wu, Z.W., Yang, T.J., Li, D.S., Ren, Y.Z., Liu, Q.F., Zhu, K.J., Yu, H.J., 2018. Mineralogy of Bi-sulfosalts and tellurides from the Yaoan gold deposit, southwest China: metallogenic implications. Ore Geol. Rev. 98, 126–140.